



Cite this: DOI: 10.1039/c7ta03162a

Impact of air exposure and surface chemistry on Li–Li₇La₃Zr₂O₁₂ interfacial resistance†

Asma Sharafi,^a Seungho Yu,^a Michael Naguib,^b Marcus Lee,^a Cheng Ma,^c Harry M. Meyer,^b Jagjit Nanda,^b Maiofang Chi,^c Donald J. Siegel^a and Jeff Sakamoto^{*a}

Li₇La₃Zr₂O₁₂ (LLZO) is a promising solid-state electrolyte that could enable solid-state-batteries (SSB) employing metallic Li anodes. For a SSB to be viable, the stability and charge transfer kinetics at the Li–LLZO interface should foster facile plating and stripping of Li. Contrary to these goals, recent studies have reported high Li–LLZO interfacial resistance which was attributed to a contamination layer that forms upon exposure of LLZO to air. This study clarifies the mechanisms and consequences associated with air exposure of LLZO; additionally, strategies to minimize these effects are described. First-principles calculations reveal that LLZO readily reacts with humid air; the most favorable reaction pathway involves protonation of LLZO and formation of Li₂CO₃. X-ray photoelectron spectroscopy, scanning electron microscopy, Raman spectroscopy, and transmission electron microscopy were used to characterize the surface and subsurface chemistry of LLZO as a function of relative humidity and exposure time. Additionally, electrochemical impedance spectroscopy was used to measure the Li–LLZO interfacial resistance as a function of surface contamination. These data indicate that air exposure-induced contamination impacts the interfacial resistance significantly, when exposure time exceeds 24 h. The results of this study provide valuable insight into the sensitivity of LLZO to air and how the effects of air contamination can be reversed.

Received 11th April 2017
Accepted 6th June 2017

DOI: 10.1039/c7ta03162a

rsc.li/materials-a

1. Introduction

The energy density and safety of batteries are critical factors in the commercialization of electric vehicles (EVs). Li-ion batteries are the incumbent battery chemistry. The implementation of EVs will benefit immensely, however, from an increase in energy storage density, beyond what is possible with Li-ion cells. One approach to achieve this goal is to use metallic Li as the anode. Compared to conventional graphite-based anodes (volumetric capacity 330 mA h cm⁻³), a metallic Li anode would enable an eightfold increase in the volumetric capacity (2760 mA h cm⁻³). This would lead to batteries with energy densities exceeding 1000 W h L⁻¹, or a 100% improvement over Li-ion cells.¹

Despite these benefits, non-uniform deposition and dendrite formation at the anode during cycling has limited the use of metallic Li when paired with liquid electrolytes. The coupling of

solid-state electrolytes (SSE) with metallic Li anodes has recently emerged to potentially resolve the dendrite issue. For example, the garnet-type Li-ion conductor, Li₇La₃Zr₂O₁₂ (LLZO), exhibits a unique combination of high ion-conductivity (1 mS cm⁻¹ at 298 K) and wide electrochemical window.^{2,3} Additionally, LLZO has a shear modulus that is 14 times higher than metallic Li, suggesting that it could act as a physical barrier to suppress dendrite formation.⁴

While LLZO exhibits favorable transport and mechanical properties, its stability in air, and the consequences of air exposure on resistance at LLZO–electrode interfaces, are not well understood. To compete with conventional Li-ion batteries, the Li–LLZO interfacial resistance should be lower than 100 Ω cm².^{5–9} Recent experimental and theoretical studies indicate LLZO indeed reacts with air, although subtly, but enough to dramatically affect the interface resistance.^{10–14}

Different pathways have been proposed to describe the reaction between air and LLZO. Studies on Li₅La₃M₂O₁₂ (M = Nb, Ta) and Li₇La₃M₂O₁₂ (M = Sn, Zr) exhibited spontaneous Li⁺/H⁺ ion exchange when exposed to water.^{12,15–17} It was shown that water reacts with LLZO to form LiOH either as a surface film (when exposed to moist air), or as a precipitate in solution (when immersed in water). Any LiOH that formed would subsequently react with CO₂ in air to form Li₂CO₃.^{15,18} Conversely, other studies reported a single-step reaction

^aMechanical Engineering Department, Materials Science & Engineering, and Applied Physics Program, University of Michigan, Ann Arbor, Michigan 48109, USA. E-mail: jeffsaka@umich.edu

^bMaterials Science and Technology Division, Oak Ridge National Laboratory, Oak Ridge, TN, USA

^cCenter for Nanophase Materials Sciences, Oak Ridge National Laboratory, Oak Ridge, TN, USA

† Electronic supplementary information (ESI) available: Other XPS core level and TEM for LLZO with longer exposure time. See DOI: 10.1039/c7ta03162a

pathway where the garnet reacts directly with water and CO_2 to form Li_2CO_3 .^{10,14} More recently, Cheng *et al.* reported that LLZO reacts with water to form Li deficient garnet and LiOH, without Li^+/H^+ ion exchange.¹⁰ Cheng *et al.* suggested that Li_2CO_3 formation can either occur through CO_2 absorption by LiOH or the direct reaction of LLZO with CO_2 . It was suggested that direct reaction of LLZO with CO_2 is the energetically-preferred reaction pathway. Additionally, Cheng *et al.* reported the presence of Li_2CO_3 as an insulating layer on the LLZO surface after processing in air led to high interfacial resistance at the Li-LLZO interface.¹⁰

Though previous work confirms LLZO reacts with air, it is clear that consensus regarding the reaction pathway has not been achieved. Clarifying the reaction pathway and how the reaction products affect the Li-LLZO interfacial resistance will facilitate technological maturation. Moreover, a better understanding of the effect of relative humidity (RH) and exposure time on the extent and consequences of these reactions would be very helpful. Such information could be useful in developing methodology to establish consistent Li-LLZO interfacial resistance when assembling solid-state cells.

This study aims to clarify the effects of RH and air exposure time with changes in LLZO surface chemistry and Li-LLZO interfacial resistance using a combination of computational modeling and experimental measurements. First, density functional theory (DFT) was used to investigate the reaction between LLZO and air. Previous DFT calculations examined the carbonation of LLZO *via* formation of LiOH or by direct reaction of LLZO with CO_2 .^{18,19} The present study takes a different approach by exploring a hydration/carbonation reaction pathway that involves Li^+/H^+ ion exchange;^{19,20} such ion exchange has been demonstrated to be facile, for example, in aqueous environments.²⁰ In addition, comparisons are made with pathways involving direct reaction of LLZO with CO_2 and H_2O . Our DFT calculations indicate that the Li^+/H^+ ion exchange pathway is a thermodynamically favorable route for the formation of a Li_2CO_3 layer on the surface of LLZO. On the other hand, direct hydration and carbonation of LLZO is found to be thermodynamically unfavorable.

Experimental measurements were performed on LLZO samples exposed for up to 240 h in air with relative humidities (RHs): ambient air (RH \sim 50%) and Li-ion battery fabrication dry room air (RH \sim 0.5%). The resulting changes in surface chemistry were characterized using X-ray photoelectron spectroscopy (XPS), scanning electron microscopy (SEM), Raman spectroscopy, and transmission electron microscopy (TEM). These analyses suggest a reaction pathway resulting in the formation of a Li_2CO_3 contamination layer on LLZO. Moreover, the growth rate of Li_2CO_3 on LLZO can be correlated with air exposure time and RH.

The impact of surface contamination on the Li-LLZO interfacial resistance was explored by electrochemical impedance spectroscopy (EIS). We find that contamination layers formed on the LLZO surface changed the chemistry of the Li-LLZO interface and contribute to an increase in the interfacial resistance. For example, air exposure for 240 h resulted in a significant increase in resistance, from 54 (no exposure) to \sim 3000 and

\sim 37 000 $\Omega \text{ cm}^2$ for air with 0.5 and 50% relative humidity, respectively. Thus, higher RH has a profound effect on Li-LLZO interfacial resistance.

Through combined theory, materials characterization, and electrochemical analysis, LLZO reactivity with air as a function of time and relative humidity is elucidated. It will be shown that LLZO can withstand exposure to ambient air (RH \sim 50 %) for up to 24 h and maintain reasonable Li-LLZO interfacial resistances. The knowledge gained could support efforts to develop approaches to fabricate solid-state battery technology in ambient air, which could significantly simplify and reduce the cost of production.

2. Experimental

2.1 Powder synthesis and pellet processing of solid-state electrolyte

Cubic Al-doped LLZO with nominal composition of $\text{Li}_{6.25}\text{Al}_{0.25}\text{La}_3\text{Zr}_2\text{O}_{12}$ was prepared using solid-state synthetic technique. Li_2CO_3 (1 μm , Alfa Aesar, Ward Hill, MA), $\text{La}(\text{OH})_3$ (1 μm , Alfa Aesar, Ward Hill, MA), Al_2O_3 (0.05 μm , Mager Scientific Inc., Dexter, MI), and ZrO_2 nanopowder (30–60 nm, Inframat, Advanced Materials, Manchester, CT) were weighed in stoichiometric ratios, and thoroughly mixed with a planetary ball mill (PM 100; Retsch, Haan, Germany). 0.25 mole of Al was added to stabilize the cubic phase at room temperature. The mixture was cold-pressed into pellets with 25.3 mm diameter in a stainless-steel die (MTI Corporation, Richmond, CA) with 8000 N force for 2 min. The cold-pressed pellets were placed in a tubular furnace (Carbolite LTD, Derbyshire, UK) and calcined at 1000 $^\circ\text{C}$ for 4 h under 2 L min^{-1} flowing dry air. All syntheses were carried out in MgO boat to prevent any unwanted Al doping of the LLZO powder during calcination process. After grinding and sieving, the calcined powder was hot-pressed into pellets with 12.7 mm diameter at 1100 $^\circ\text{C}$ and 62 MPa pressure for 1 h under argon flow by rapid induction hot press (RIHP, Across International, Livingston NJ) in graphite die to achieve $97 \pm 1\%$ relative density and eliminate the effect of volume percent of porosity on the results. The hot-pressed pellets were cut into 1 ± 0.2 mm thick samples using diamond saw (Buehler, Lake Bluff, IL). Samples were mechanically polished using 400 grit sandpapers (Norton Abrasives, Worcester, MA) to ensure both faces were parallel, then all the LLZO were transferred to an argon-filled glovebox with <0.1 ppm oxygen level. To characterize the stability of LLZO against air and moisture, each sample was dry-polished with 400, 600, 1500 and 2000 grit SiC sandpapers inside an argon-filled glovebox to remove the entire contamination layer formed during processing and achieve a well-defined fresh surface, which had not been in contact with air before. Then, the LLZO were exposed to ambient air with 50% RH, and dry air with 0.5% RH and -40 $^\circ\text{C}$ dew point for duration between 0 to 240 h.

2.2 Calculations

The thermodynamics of the hydration and carbonation of LLZO were examined using first-principles calculations. All

calculations were conducted using Density Function Theory (DFT) with a plane wave basis set, as implemented in the Vienna *Ab initio* Simulation Package (VASP).²¹ Core-valence electron interactions were treated using the projector augmented wave (PAW) method.^{22,23} The generalized gradient approximation (GGA) of Perdew, Burke, and Ernzerhof (PBE) was used for the exchange–correlation energy.²⁴ The convergence criterion for the electronic self-consistency loop was set to 10^{-5} eV, and ionic relaxations were converged to a force tolerance of less than $0.03 \text{ eV } \text{Å}^{-1}$. An energy cut-off 600 eV was used for the plane wave basis and the Brillouin zone was sampled using the Monkhorst–Pack scheme. A $2 \times 2 \times 2$ *k*-point grid was used for LLZO, and $12 \times 12 \times 12$ *k*-point mesh was used for crystalline LiOH, Li₂O, and Li₂CO₃.

The conventional cubic unit cell of Li₇La₃Zr₂O₁₂ (8 formula units, 192 atoms) was adopted as the simulation cell.²⁵ Lithium was distributed on the partially-occupied 24 d and 96 h Li-sub lattice sites according to an algorithm that minimizes occupancy of electrostatically-unfavorable first nearest-neighbor sites.²⁵ An earlier study showed negligible energy differences (<1.5 meV per atom) amongst several LLZO structures generated using this procedure.²⁵ The LLZO structure having the lowest total energy (with 13 and 43 atoms occupying the 24 d and 96 h Li sites, respectively) was adopted for subsequent calculations.

Calculations on hydrogen-doped LLZO were performed by substituting hydrogen atoms for selected Li atoms. A prior experimental study of proton exchange in LLZO reported that proton substitution preferentially occurs on the 96 h sites.^{26,27} Our DFT calculations are consistent with the site preference observed experimentally: at low proton concentrations (2% and 9% Li⁺/H⁺ exchange) 96 h sites are favored over 24 d sites by 1 to 8 meV per atom. At higher concentrations (~63% Li⁺/H⁺ exchange) the preference for the 96 h sites increases to ~20 meV per atom.

The molecular species H₂O and CO₂ were simulated within cubic simulation cells with dimensions of 8 Å; crystal structures for LiOH, Li₂O, and Li₂CO₃ were taken from experimental data.²⁸ The optimal lattice parameters for all computational cells were obtained by fitting total energy vs. volume data to the Murnaghan equation of state.²⁹

The Gibbs free energies of gas and liquid phases were obtained using eqn (1) and (2):

Gas phase:

$$G(T) = E_{0 \text{ K(g)}}^{\text{DFT}} + \Delta H(T) - TS_{(\text{g})}^{\text{expt}}(T) \quad (1)$$

Liquid phase:

$$G(T) = E_{0 \text{ K(g)}}^{\text{DFT}} + \Delta H(T) - \Delta H_{\text{vap}}^{\text{expt}}(T) - TS_{(\text{l})}^{\text{expt}}(T) \quad (2)$$

here $E_{0 \text{ K(g)}}^{\text{DFT}}$ is the total energy of an isolated gas phase molecule at zero Kelvin, $\Delta H(T)$ is the enthalpy difference for the molecule associated with a temperature change between 0 K and a given temperature *T*, $S_{(\text{i})}^{\text{expt}}$ is the experimental gas (*i* = g) or liquid (*i* = l) phase entropy at temperature *T*,³⁰ and $\Delta H_{\text{vap}}^{\text{expt}}(T)$ is the experimental enthalpy of vaporization.³¹ The ideal gas approximation was used to estimate the enthalpy difference, $\Delta H(T) \approx nk_{\text{B}}T$, where *n* is 7/2 for linear molecules (*i.e.*, CO₂) and 4 for nonlinear

molecules (*i.e.*, H₂O), respectively. The pressure was set to 1 atm. Finally, the Gibbs free energies of solids were approximated as the DFT total energy, $G \approx E_{0 \text{ K}}^{\text{DFT}}$.

2.3 Materials characterization

The formation and morphology of contamination layers after air exposure was examined using scanning electron microscopy, and their elemental composition was determined by energy-dispersive X-ray spectroscopy (SEM/EDS, FEI Nova 200 Nano Lab Dualbeam, Hillsboro, OR) at an accelerating voltage of 10 kV and a working distance of 5 mm.

Raman spectroscopy (Renishaw inVia Raman microscope, Hoffman Estates, IL) was performed using a 532 nm laser, 2400 lines per mm holographic grating and 50× magnification using power of 100 mW to determine the surface composition and chemistry. All the intensity profiles were normalized by the corresponding maximum values. Direct Classical Least Squares (DCLS) method was used to determine the quantitative analysis of Raman spectroscopy regarding the LLZO surface constituent properties. DCLS finds the combination of spectra from the pure components contained in the sample that more closely matches the Raman spectrum of the sample. Reference spectra for all the possible component of the surface (*i.e.* cubic LLZO, Li₂CO₃ and LiOH) were acquired. The DCLS method approximates the spectrum at each point in the map by adding the entire scaled reference spectrum. The scaling factors helped to get the best fit to the original map to show the distribution of each reference spectrum.

The subsurface composition based on the degree of air exposure was evaluated using scanning transmission electron microscopy (STEM) and electron energy loss spectroscopy (EELS). TEM technique (STEM/EELS, an aberration-corrected FEI Titan S 80-300 TEM/STEM, Hillsboro, OR) equipped with a Gatan Image Filter Quantum-865 operated at 300 kV. Z-Contrast HAADF-STEM imaging was performed with a probe convergence angle of 30 mrad and a large inner collection angle of 65 mrad. EELS data were collected in STEM mode using a 5 mm aperture and a spectrometer collection angle of 40 mrad. Before being exposed to ambient air, a LLZO was split into two pieces to create a fresh surface for this study. After 24 h exposure, the cross-section surface then was coated with a ~40 nm gold layer followed with a thick tungsten layer on surface. The TEM specimen was then prepared by using a Hitachi NB-5000 dual (Focused Ion/Electron) beam microscope. When the specimen was properly prepared, it was transferred into a vacuum transfer TEM holder inside the FIB. The specimen is finally transferred to an FEI double tilt holder in an argon-filled glove box before being put in the TEM.

X-ray photoelectron spectroscopy (XPS) was performed with a Thermo Scientific Model K-Alpha XPS instrument. The instrument uses a monochromated, micro-focusing, Al K_α X-ray source (1486.6 eV) with a variable spot size (30–400 μm). Analyses of LLZO samples used the 400 μm X-ray spot size for maximum signal and to obtain an average surface composition over the largest possible area. The instrument has a hemispherical electron energy analyser equipped with a 128 multi-channel detector system. The base pressure in the analysis chamber is typically 2 ×

10^{-9} mbar or lower. LLZO samples were fixed to the sample holder using metal clips. Wide energy ranges survey spectra (0–1350 eV) were acquired at an analyser pass energy of 200 eV. Narrow energy range core level spectra were acquired an analyser pass energy of 50 eV. Argon-ion depth profiling was performed using a 2 kV argon-ion beam rastered over an area 1×2 mm and alternated with core level data acquisition cycles. The depth scale was calibrated using standard SiO_2 films to measure the argon-ion gun sputter rate (note that the depth scales shown are relative to the sputter rate of SiO_2). For depth profiling a rapid data acquisition mode was used that takes a series of “snapshots” of the core level of interest across the 128-channel detector. Charging was avoided by using a charge neutralization system that uses a combination of low energy electrons and low energy argon ions for optimum charge compensation. The typical pressure in the analysis chamber with the flood gun operating was 2×10^{-7} mbar. Data were collected and processed using the Thermo Scientific Avantage XPS software package (v 4.61).

2.4 Electrochemical impedance measurement

The Li–LLZO–Li cell impedance as a function of exposure time and RH level was characterized by electrochemical impedance spectroscopy (EIS) technique between 1 Hz to 7 MHz using a 100 mV perturbation amplitude (VMP300, Bio-Logic, Knoxville, TN). The LLZO samples were transferred inside an argon-filled glovebox after air exposure for specific amount of time (0, 24, 120, 240 h) to eliminate further formation and the growth of contamination layer. Li foil (Alfa Aesar, Ward Hill, MA) was scraped using a stainless-steel spatula to remove the oxide surface layer and expose the fresh metallic Li surface. The LLZO was placed between two scrapped Li foil. Afterward, the stack was placed under uniaxial force of 365 kPa to achieve a better contact between Li and LLZO at the interface.

An equivalent circuit model was used for modeling the EIS data. The entire impedance spectrum for each cell was normalized to Li and LLZO contact area (1.26 cm^2) before the data modeling was performed. The EIS data was modeled using the equivalent circuit model shown in Fig. 7a. In this model, a combination of a resistor and a capacitor in parallel are used to represent each component in the cell. Thus, three parallel combinations were used in the model representing the bulk and the grain boundary of LLZO, and the Li–LLZO interface. The ideal capacitors were replaced with constant phase elements (CPE) to account for any non-ideal behavior and dispersion in to the time constant. The ideality of The CPE is represented by the coefficient α ($\alpha = 1$ shows the component is behaving as an ideal capacitors). The Q values for the CPE should be on the order of 10^{-12} , 10^{-8} , 10^{-6} F for bulks, grain boundaries and Li–LLZO interface, respectively.^{32,33} The data fitting and circuit modeling was done with a software package EC-Lab V10.44.

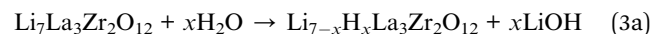
3. Results and discussions

3.1 First principle calculations

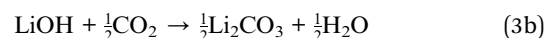
The thermodynamic driving force (*i.e.*, the Gibbs free energy of reaction, ΔG) for the hydration and/or carbonation of LLZO was

evaluated using DFT calculations for several plausible reaction pathways. The first pathway results in Li_2CO_3 formation, and proceeds *via* a two-step process that involves protonation of LLZO (*i.e.*, Li^+/H^+ exchange) and the formation of LiOH as an intermediate:^{18,34}

Li^+/H^+ ion exchange:

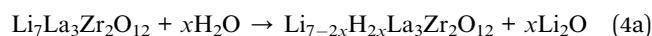


Carbonation of LiOH:

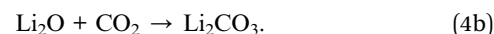


In a similar fashion, the second pathway also results in LLZO protonation and formation of Li_2CO_3 , but proceeds through an Li_2O intermediate:

Li^+/H^+ ion exchange:

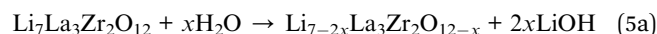


Carbonation of Li_2O :



Finally, the energetics of direct hydration and carbonation of LLZO were also investigated:

Direct hydration:



Direct carbonation:

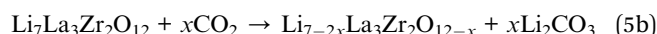


Table 1 summarizes the calculated ΔG for reactions (3)–(5) with $x = 1/8$ at $T = 298.15 \text{ K}$ (here $x = 1/8$ refers to the exchange of a single Li^+ for H^+ in the LLZO computational cell for reactions 3a–b to the exchange of two Li^+/H^+ pairs for reactions 4a–b, and to the extraction of a single formula unit of Li_2O in reactions 5a–b). Several configurations were examined for the substitution and extraction of these species; the lowest energy configurations were used to evaluate eqn (3)–(5). Overall, pathway (3a) and (3b) (involving protonation of LLZO and formation of an LiOH intermediate) is predicted to be the most thermodynamically favorable reaction, given the negative values calculated for ΔG , -33 kJ mol^{-1} for reaction (3a) and -34 kJ mol^{-1} for (3b). These data are in good qualitative agreement with experimental measurements that report Li^+/H^+ ion exchange and Li_2CO_3 formation in ambient air.¹⁸ On the other hand, pathway (4a) and (4b) (involving protonation of LLZO and formation of an Li_2O intermediate) is somewhat less favored due to the positive reaction energy of 21 kJ mol^{-1} predicated for its first step, reaction (4a). In addition, the total reaction energy for pathway (4), -127 kJ per Li_2CO_3 formula unit (f.u.), is less exergonic than that of reaction (3): -134 kJ per Li_2CO_3 f.u. Finally, formation of LiOH and Li_2CO_3 by the direct reaction of LLZO with H_2O or CO_2 (eqn (5a) and (5b)) is predicted to be thermodynamically unfavorable, as $\Delta G > 0$ for both reactions ($\Delta G = 83 \text{ kJ mol}^{-1}$ for reaction (5a) and 15 kJ mol^{-1} for (5b)).

Table 1 Calculated Gibbs free energy for the hydration and carbonation of LLZO depicted in reactions (3)–(6) with $x = 1/8$ at 298.15 K for reactions involve Li^+/H^+ ion exchange (*i.e.*, protonation) and formation of an LiOH (reaction (3(a) and 3(b)) or an Li_2O (reaction (4(a) and 4(b)) intermediate phase. Reactions (5(a) and 5(b)) assume direct hydration and carbonation of LLZO. Reaction (6) depicts the thermal decomposition of Li_2CO_3 in the presence of protonated LLZO

Reaction no.	Reaction (assuming $x = 1/8$)	$\Delta G/\text{kJ mol}^{-1}$
3(a)	$\text{Li}_{56}\text{La}_{24}\text{Zr}_{16}\text{O}_{96} + \text{H}_2\text{O}(\text{g}) \rightarrow \text{Li}_{55}\text{HLa}_{24}\text{Zr}_{16}\text{O}_{96} + \text{LiOH}$	-33.0
3(b)	$\text{LiOH} + \frac{1}{2}\text{CO}_2(\text{g}) \rightarrow \frac{1}{2}\text{Li}_2\text{CO}_3 + \frac{1}{2}\text{H}_2\text{O}(\text{g})$	-33.6
4(a)	$\text{Li}_{56}\text{La}_{24}\text{Zr}_{16}\text{O}_{96} + \text{H}_2\text{O}(\text{g}) \rightarrow \text{Li}_{54}\text{H}_2\text{La}_{24}\text{Zr}_{16}\text{O}_{96} + \text{Li}_2\text{O}$	+21.5
4(b)	$\text{Li}_2\text{O} + \text{CO}_2(\text{g}) \rightarrow \text{Li}_2\text{CO}_3$	-147.6
5(a)	$\text{Li}_{56}\text{La}_{24}\text{Zr}_{16}\text{O}_{96} + \text{H}_2\text{O}(\text{g}) \rightarrow \text{Li}_{54}\text{La}_{24}\text{Zr}_{16}\text{O}_{95} + 2\text{LiOH}$	+82.8
5(b)	$\text{Li}_{56}\text{La}_{24}\text{Zr}_{16}\text{O}_{96} + \text{CO}_2(\text{g}) \rightarrow \text{Li}_{54}\text{La}_{24}\text{Zr}_{16}\text{O}_{95} + \text{Li}_2\text{CO}_3$	+15.6
6	$\text{Li}_{55}\text{HLa}_{24}\text{Zr}_{16}\text{O}_{96} + \frac{1}{2}\text{Li}_2\text{CO}_3 \rightarrow \text{Li}_{56}\text{La}_{24}\text{Zr}_{16}\text{O}_{96} + \frac{1}{2}\text{H}_2\text{O}(\text{g}) + \frac{1}{2}\text{CO}_2(\text{g})$	+66.6

Fig. 1a plots ΔG at $T = 298.15$ K for reaction (3(a)) as a function of the Li^+/H^+ exchange percentage. The data reveals that Li^+/H^+ ion exchange is thermodynamically favorable for all proton compositions up to full exchange of Li^+ . The most negative ΔG value occurs at approximately 80% protonation; this value is in reasonable agreement with an earlier experimental study that observed approximately 60% of Li in LLZO powder could be exchanged with hydrogen in de-ionized water at room temperature.^{20,26} Although ΔG is negative for all proton concentrations, limited Li^+/H^+ ion mobility within partially ion-exchanged LLZO could kinetically preclude achieving very high (or full) proton exchange.²⁰

Fig. 1b plots ΔG for reaction (3(a)) (assuming $x = 1/8$) as a function of temperature and the phase of the proton source,

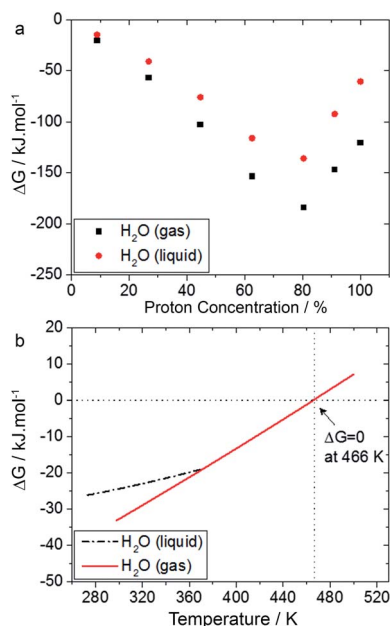
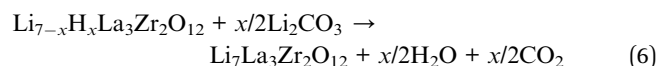


Fig. 1 DFT calculations to evaluate the reactivity between ambient and LLZO. (a) The change in Gibbs free energy at 298.15 K for reaction (3(a)) as a function of proton concentration, (b) the change in Gibbs free energy for LLZO protonation, reaction (3(a)), as a function of temperature and the phase of the proton source (liquid or gaseous H_2O). The calculation assumes $x = 1/8$.

liquid or gaseous water. The data reveals that reaction (3(a)) is favorable at low-to-moderate temperatures, $\Delta G < 0$ up to 466 K, regardless of whether water is a liquid or vapor. At higher temperatures, the positive values of ΔG for reaction (3(a)) indicate the possibility for reversing the effects of water exposure by decomposing LiOH and de-protonating LLZO. In addition, we investigated the possibility for thermal decomposition of Li_2CO_3 based on a pathway that is the reverse of reactions (3a) and (3b):



As before, we assume $x = 1/8$ (the exchange of a single Li^+ for H^+ in the LLZO unit cell). The energetics associated with reaction (6) at $T = 298.15$ K are summarized in Table 1. Our calculations indicate that reaction (6) becomes thermodynamically favorable at 597 K, suggesting the possibility for decomposition of Li_2CO_3 and de-protonation of LLZO at high temperatures. Our predicted decomposition temperatures are consistent with earlier TG-MS measurements showing H_2O evolution from LLZO at approximately 523 K, and de-protonation of LLZO with decomposition of Li_2CO_3 between 673 and 773 K.^{18,34}

3.2 XPS depth profiling analysis

To elucidate the details of the reaction between LLZO and air, experiments were conducted to compliment the DFT calculations. First, XPS was conducted on the LLZO to determine the dominant surface species and evaluate if these species were consistent with the results of DFT calculations. Chemical stability and surface reactivity of LLZO after initial processing in ambient air ($\text{RH} \sim 50\%$) was studied using XPS. The initial processing includes hot-pressing, cutting and dry polishing in ambient air prior to transferring into the argon-filled glovebox. XPS depth profiling analysis was performed using an argon-ion sputtering source. Fig. 2a and b show the typical carbon and Li 1s core level spectra at different sputter depths (time intervals) with 0 nm corresponding to zero sputtering time (Information regarding other core levels can be found in the ESI Fig. S1†). The depth profiling analysis of all the core levels as a function of thickness is presented in Fig. 2c. At 0 nm, we find two primary

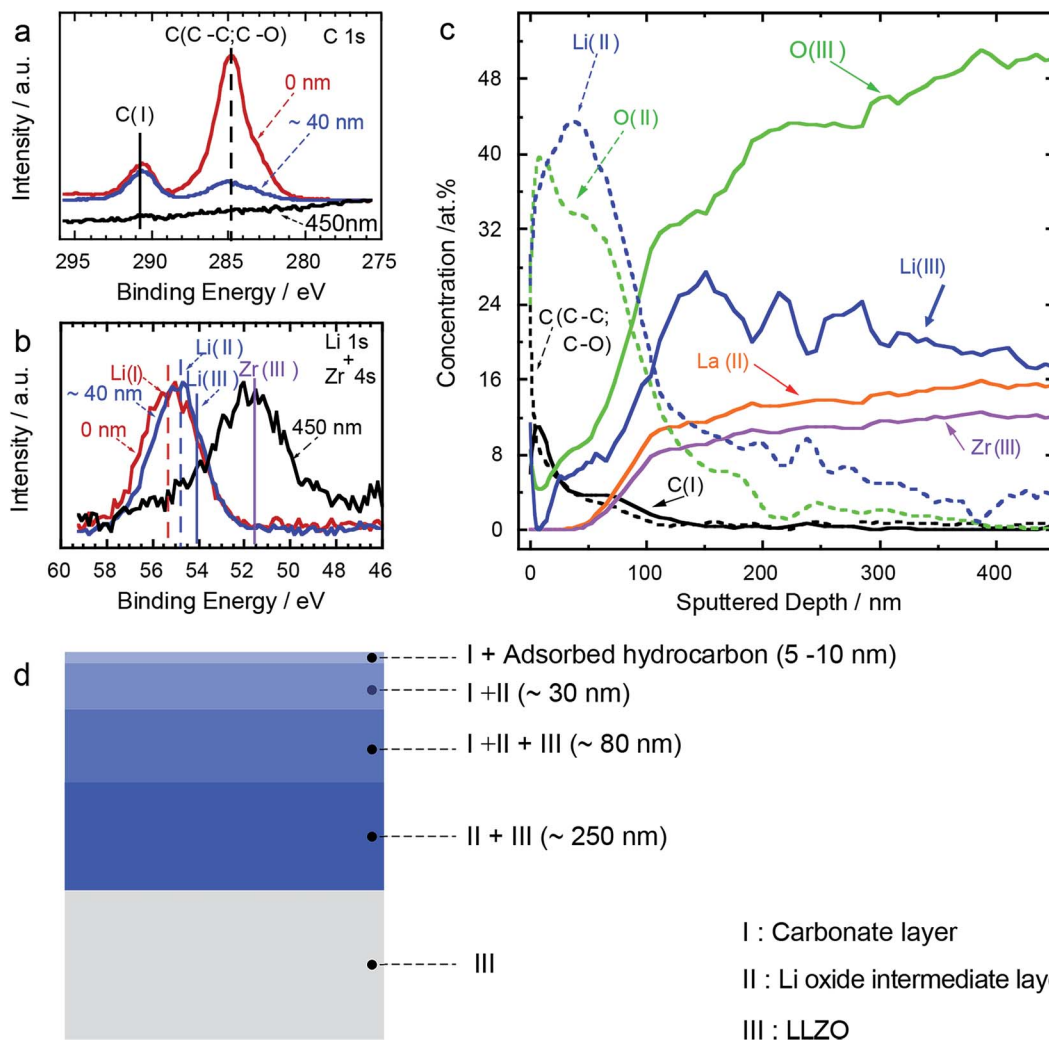


Fig. 2 XPS analysis of LLZO after sample preparation in ambient air. (a) C 1s and (b) Li 1s + Zr 4s at different sputtering depths. (c) Depth profile for the concentration of Li, C, O, Zr, La from the XPS core levels analysis. (d) Schematic depicting the contamination layers that comprise the xps analysis (the numbers between parenthesis represent the layer thickness estimated from the depth profile).

carbon components with a larger intensity peak at a binding energy (BE) of 284.8 eV corresponding to adsorbed hydrocarbons and another at higher BE peak at 290 eV attributed to carbonate species. Consistent with C 1s core level, the O 1s signal (Fig. S1b[†]) also shows two features. The adsorbed hydrocarbons were readily removed as evidenced by the diminishing C 1s peak down to 40 nm, but still substantial carbonate species were present. Upon sputtering 100's of nm below the surface, the carbonate layer is completely removed as shown by the black spectrum in Fig. 2a at 450 nm. Consistent with this observation, the Li 1s core level corresponding to the pure carbonate component is at 55 eV at 0 nm and then progressively moves towards lower BE at higher sputtering times, finally overlapping with the relatively strong Zr 4s signal at 450 nm (Fig. 2b). Based on the relative intensity variation of Li, C, O, Zr, La XPS core levels as a function of sputtering depth, the LLZO atomic compositions at various depths can be determined as summarized in Fig. 1c (see ESI for more details[†]). The respective elemental core levels are marked by (I), (II) and

(III) for carbonate, intermediate oxide/hydroxide, and LLZO, respectively.

The carbonate was present up to 5–10 nm beneath the surface then decreased gradually reaching the minimum concentration at about 40 nm. This gradual decrease in carbonate content was accompanied by an increase in the Li oxide/hydroxide, Li(II), suggesting a buried oxide/hydroxide layer. However, the difference in BE values for Li 1s between the oxide *versus* hydroxide is relatively small and difficult to deconvolute. Sputtering deeper than 40 nm (in the region between 40 to 100 nm) revealed a decrease in the Li(II) content with a gradual increase in the La and Zr concentration. It is worth noting that in the region between 40 to 120 nm, the three components (carbonate, Li oxide/hydroxide and LLZO) are simultaneously present. In this region, the pristine or bulk LLZO content gradually increases while both the carbonate and Li oxide/hydroxide concentrations diminished with increasing sputtering depth. It is important to note that given the weak XPS cross-section for Li, a relatively large uncertainty for

determining the Li composition is expected compared to other easier to detect core levels. Furthermore, in bulk LLZO regions the Li 1s substantially overlaps with Zr 4s complicating the analysis. The schematic in Fig. 2d summarizes the findings described above. These findings show the surface of LLZO is readily contaminated during processing and preparation in air. To further explore the implications of these results, more detailed experiments were carried out to probe the effect of RH and time on the surface chemistry and topography upon gradual exposure of LLZO to air. To this end, the LLZO samples were polished and stored in an argon-filled glovebox to remove the contamination layer formed on the surface during processing and exposed to ambient (RH ~ 50%) and dry air (RH ~ 0.5%) for various times.

3.3 SEM/EDS mapping characterization

To characterize the LLZO surface chemistry and topography upon air exposure, SEM was conducted before and after 240 h of air exposure at RH ~ 50%, Fig. 3. From Fig. 3, several observations can be made. First, the SEM of the polished LLZO surface with no exposure confirms the uniform morphology where the only features present are the polishing lines (Fig. 3a). Second, a noticeable change in surface topography is apparent as shown in Fig. 3b, which is evidence of the secondary phase formation upon prolonged air exposure. The topography changes morphology in stages, first as continuous layers followed by the formation of nodular features. The nodular features, indicated by the arrows in Fig. 3c, are evidence of non-uniform growth on the LLZO surface. To evaluate the chemical composition of these surface features, energy-dispersive X-ray spectroscopy (EDS) was conducted on a specific region marked by a square in Fig. 3b. The related EDS maps for Zr, La, O, and C are shown in Fig. 3e–g. The analysis of the surface composition showed a decrease in La and Zr on the micron size features, Fig. 3c. On the other hand, the O and C contents were much higher in the

same regions. The EDS spectra, as shown in Fig. 3d also contains C, which is believed to be contained within the Li_2CO_3 layer. SEM/EDS mapping confirmed that the contamination layer was non-uniform in thickness and density. Further investigations are required to evaluate the cause of this non-uniformity.

3.4 Raman spectroscopy and mapping

While EDS analysis provides elemental distribution, correlating the features with stoichiometric compounds requires a complementary analytical technique. To determine the compounds present, Raman spectroscopy was used. The Raman spectra shown in Fig. 4a were collected from the surface of LLZO after exposure to ambient and dry air for various times ranging between 0 to 240 h. The Raman spectrum of cubic LLZO with 0 h air exposure agrees well with the spectra reported in literature.^{18,35–37} The Raman spectrum for LLZO can be divided into three regions; a low-energy region ($<300\text{ cm}^{-1}$), an intermediate-energy region ($300\text{--}550\text{ cm}^{-1}$), and a high-energy region ($>550\text{ cm}^{-1}$) attributed to the vibration of the heavy La cations, Li vibrations and the vibrational stretching modes of ZrO_6 octahedral units, respectively. It is believed that the 1100 cm^{-1} peak can be assigned to Li_2CO_3 . The presence of Li_2CO_3 is consistent with previous reports by Larraz *et al.* and Cheng *et al.*^{10,18} In addition, our DFT calculations confirm the reaction between ambient air and LLZO. In Fig. 4a, the carbonate peak intensity at 1100 cm^{-1} increased with exposure time, indicating growth of a carbonate layer on LLZO surface. In addition, the lower intensity Li_2CO_3 peak at 1100 cm^{-1} for LLZO exposed to dry air (RH ~ 0.5%) in comparison with ambient air (RH ~ 50%) for the same amount of exposure time suggests that the moisture content during exposure plays a significant role in the formation rate of Li_2CO_3 on the LLZO surface.

LiOH is another expected phase to appear on LLZO surface upon air exposure.^{10,18} However, there is an overlapping feature

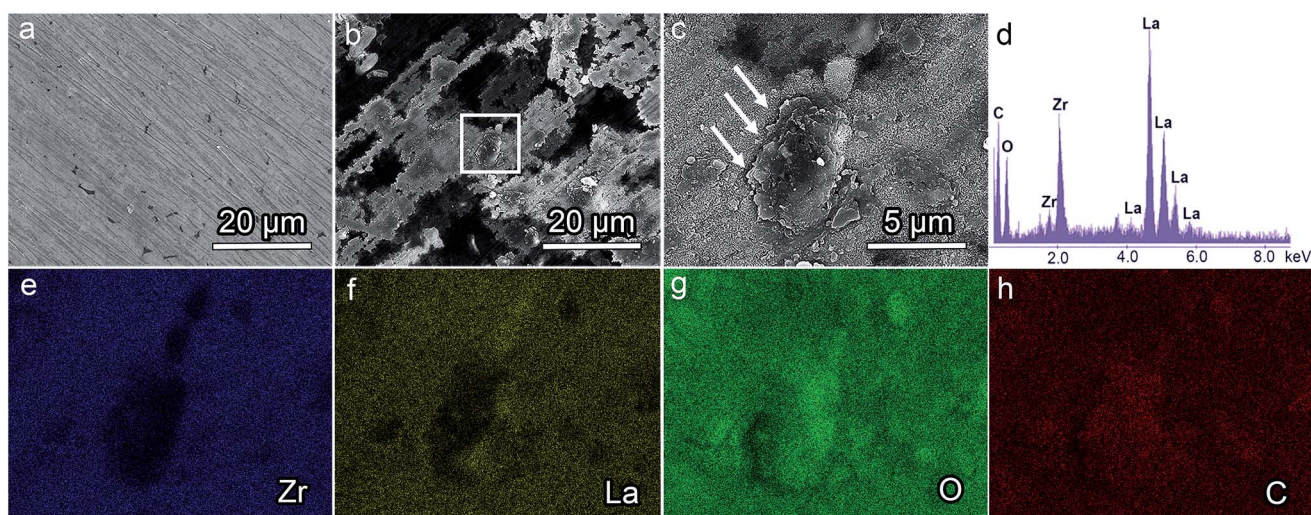


Fig. 3 Secondary SEM micrographs of the LLZO surface. (a) Before air exposure air, (b) after exposure to ambient air, (c) enlarged SEM micrograph of dotted box in (b), (d) the EDS spectrum of the LLZO surface layer and the corresponding EDS mapping of (e) Zr, (f) La, (g) O, (h) C.

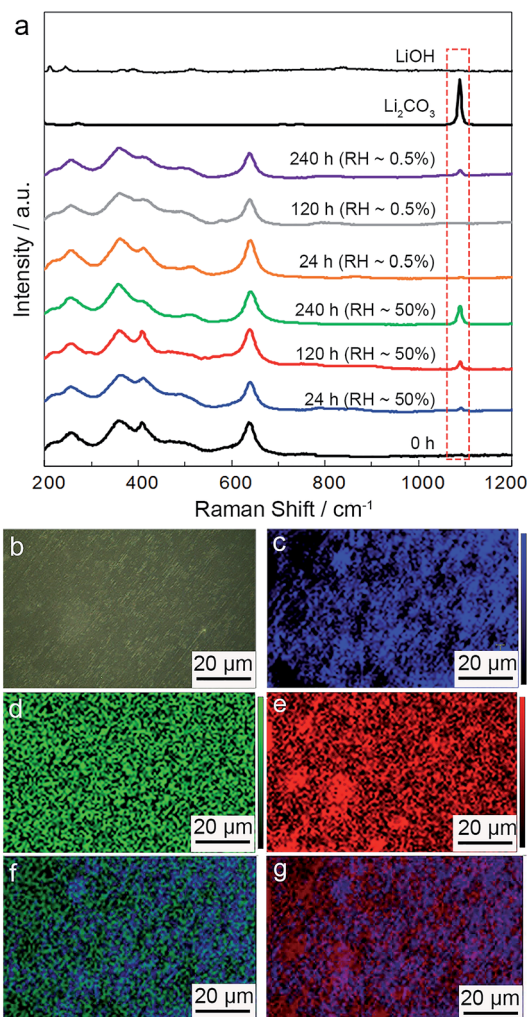


Fig. 4 Raman analysis of LLZO before and after exposure to ambient and dry air (a). The dotted line highlights growth of the Li_2CO_3 layer on LLZO as a function of exposure time and RH. Topographic analysis of LLZO exposed to air (RH = 50%) for 240 h. (b) Optical image of LLZO, Raman mapping of: LLZO (c), LiOH (d), Li_2CO_3 (e), the overlay of LLZO (blue) and LiOH (green) (f), the overlay of LLZO (blue) and Li_2CO_3 (red), and (g) to show the distribution of different phases on the surface.

in the Raman spectra for LiOH and the vibration of La cations in LLZO at lower frequency with Raman shift in a range of 210–250 cm^{-1} making deconvolution of these spectra difficult. Hence, Raman mapping and DCLS modeling were used to confirm the existence of LiOH on the LLZO surface. Distribution maps were created to determine and evaluate the complementary information on the coverage and an estimation of the LLZO surface chemistry after air exposure for 240 h by DCLS modeling. Reference spectra of the pure component including cubic LLZO, LiOH and Li_2CO_3 were accumulated. The Raman shift at 1100 cm^{-1} allows for reliable determination of the Li_2CO_3 content with DCLS modeling, since the other phase did not have an overlapping Raman shift in this spectral region. Fig. 4 compares the spatial distribution of the LiOH and Li_2CO_3 on the LLZO surface. After prolonged exposure to ambient air, the LiOH is distributed almost equally on the LLZO surface and leading to

a homogenous distribution as shown in Fig. 4d and f. However, mapping of Li_2CO_3 indicated that the distribution of Li_2CO_3 was not uniform as shown in Fig. 4e and g. The results of Raman spectroscopy are, therefore, consistent with the results of the SEM analysis in identifying the non-homogeneous formation of the contamination layer. These results indicate that exposure of LLZO to air results in the formation of a contamination layer consisting of LiOH and Li_2CO_3 .

3.5 TEM characterization

To determine the effect of air exposure on and below the LLZO surface TEM of the LLZO cross section after exposure to ambient air was performed. Fig. 5 shows a high-angle annular dark field (HAADF) scanning TEM (STEM) image and electron energy loss spectroscopy (EELS) maps of a LLZO cross section after 24 h exposure to ambient air (RH ~ 50%). Three distinct layers can be differentiated in LLZO according to the image contrast in Fig. 5a, which will be referred to as the base, intermediate, and dark layers.

Fig. 5b–d show EELS spectra of O, Li, La, and C, respectively. The O-K edge with an onset about 525 eV for all three layers in Fig. 5b confirmed the presence of O in all three layers. Fig. 5c shows the Li-K edge peak position and amplitude varies considerably between different layers. The outermost layer, *i.e.* the dark layer, contains a significantly more Li than the other layers. In contrast, the intermediate layer has significant Li deficiency compared to base and the dark layer. Additionally, the La-N_{4,5} edge on LLZO cross section after air exposure reveals the presence of La in both base and intermediate layers, however the concentration of La in the dark layer is negligible. As the only elements detected from the dark layer are Li, C, and O, it is most likely the dark layer is Li_2CO_3 that formed during air exposure on the LLZO surface. In fact, the fine structure Li-K edge in Fig. 5c for dark layer matches those from Li_2CO_3 reported previously, confirming the formation of Li_2CO_3 .³⁸ On the other hand, the intermediate layer possesses both La and Li with significantly reduced Li content compared to the base layer. This can be attributed to the formation of Li_2CO_3 that sequestered Li and possibly some O from LLZO, leading to a phase transition and the formation of the intermediate layer beneath the Li_2CO_3 layer. Moreover, the Li depleted interlayer could be partially protonated as reported previously by Larraz *et al.* and Cheng *et al.*; Li^+/H^+ exchange occurs in this layer to maintain charge neutrality upon reaction with H_2O and CO_2 from ambient air.^{18,19} The TEM images of LLZO cross-section after 120 and 240 h air exposure are provided in ESI (Fig. S2†). These images show a considerable increase in the thickness of intermediate and dark layers. This implies the contamination layer formation continues to grow with longer exposure time.

3.6 XPS surface characterization

At the change in surface chemistry, XPS analysis was conducted again as a function of air exposure. However, compared to the analysis using the initial XPS data in Fig. 2, care was taken to clean the LLZO surface by polishing in an inert argon

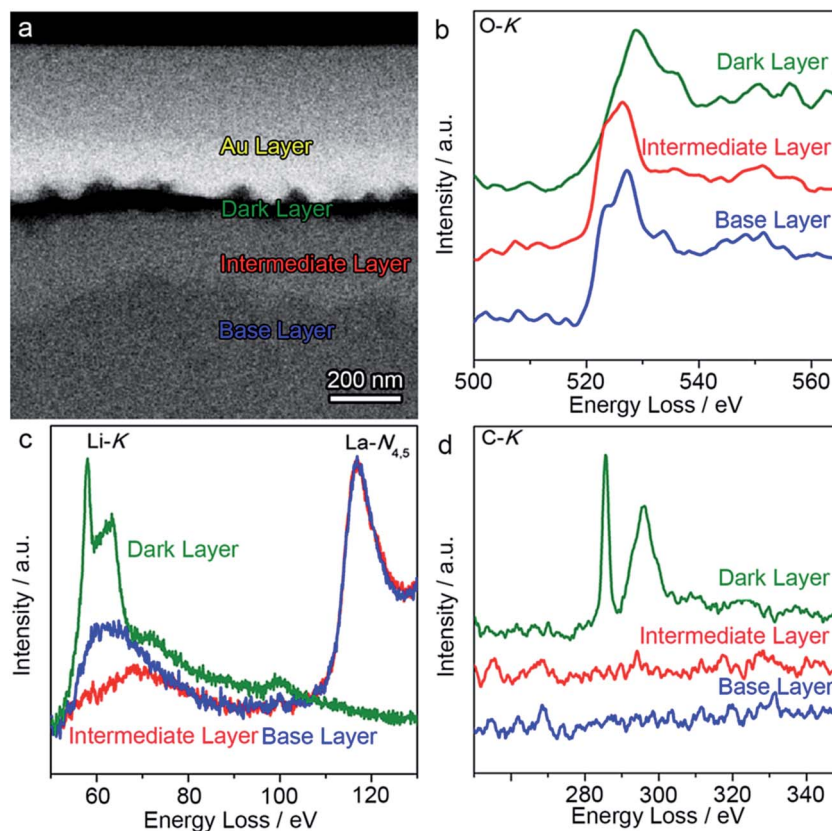


Fig. 5 Cross sectional tem image of LLZO pellet after 24 h air exposure to ambient air with 50% RH (a), and corresponding EELS maps of oxygen (O-K) (b), lithium (Li-K) and lanthanum (La-N_{4,5}) (c) and carbon (C-K) (d) on all the three layers (base layer, intermediate layer and dark layer) detected in LLZO after air exposure. The last layer above the dark layer is sputtered gold that was used to prevent electron beam damage.

atmosphere. The sample was transferred immediately after polishing into the XPS chamber using a load locker to prevent any air exposure. Initial measurements on the polished LLZO with no air exposure were made, followed by the controlled and deliberate exposure to ambient air (RH \sim 50%) for pre-determined periods. The cumulative air exposure time was 401 minutes. The results are reported in Fig. 6. For the sake of clarity, the C 1s and O 1s analysis are only shown in Fig. 6a (the XPS analysis related to Li 1s, Zr 4s, Zr 3d 1s, and La 3d_{5/2} core levels can be found in Fig. S3[†]). At $t = 0$, the C 1s core level spectra show mainly a C 1s peak at 284.8 eV that can be assigned to adventitious carbon that existed in the glovebox or in the XPS vacuum chamber. The absence of a carbonate-type peak at a BE of \sim 289 eV suggests that the LLZO surface was effectively cleaned and transferred to the XPS instrument with no exposure to air.

Additionally, the O 1s signal shows a strong peak at BE \sim 531 eV and a weaker peak at \sim 528.5 eV. The former peak was reported by Cheng *et al.* for LLZO that was polished in the glovebox, but the latter was not.¹⁹ It is worth noting that the O 1s peak for LLZO after sputtering down to \sim 450 nm (for the sample discussed above) was found to be at \sim 528 eV, which is similar to the relatively weak peak observed here. Thus, it is reasonable to conclude that the peak at 528.5 eV represents O in bulk LLZO(III), while the peak at BE \sim 531 eV represents component (II), which could be the reaction layer due to trace

amounts of oxygen in the glovebox or nominal contamination in the evacuated sample load locker. Since the XPS signal intensity decays exponentially, the surface oxide signal is masking the lattice O signal corresponding to pristine LLZO(III) at 528.5 eV. The atomic ratio of Zr to O(III) at $t = 0$ was found to be 1.0 : 3.3 (for stoichiometric LLZO, it should be 1.0 : 6.0), thus it is reasonable to assume that the extra Zr is incorporated in component (II) and the latter is not just simply Li oxide/hydroxide. With subsequent air exposure, the carbonate build up completely dominates the O 1s signal (I). Upon the initial 7 min of air exposure, clear evidence of Li₂CO₃ is detected and maintained throughout the duration of the 401 minutes cumulative time. The O 1s (I) feature corresponding to carbonate also grows concomitantly (Fig. 6a, right panel).

Fig. 6b shows XPS core levels spectra for C, O, Li, Zr, and La features vs. cumulative exposure time. These features are based on peak fittings as discussed above. For the spectrum acquired at 161 minutes of air exposure, if the C, O, and Li values are normalized using the C value, it is clear the overall stoichiometry is close to Li₂CO₃. Hence, it can be deduced that the material growing on the surface due to exposure to air is Li₂CO₃. The same investigation was done for Li 1s, Zr 4s, Zr 3d and La 3d_{5/2} core level for exposure time between 0 to 401 minutes (Fig. S3[†]). The Zr and La features quickly diminished with air exposure and again are not detectable after 161 minutes of air exposure. This indicates that this period was sufficient to form

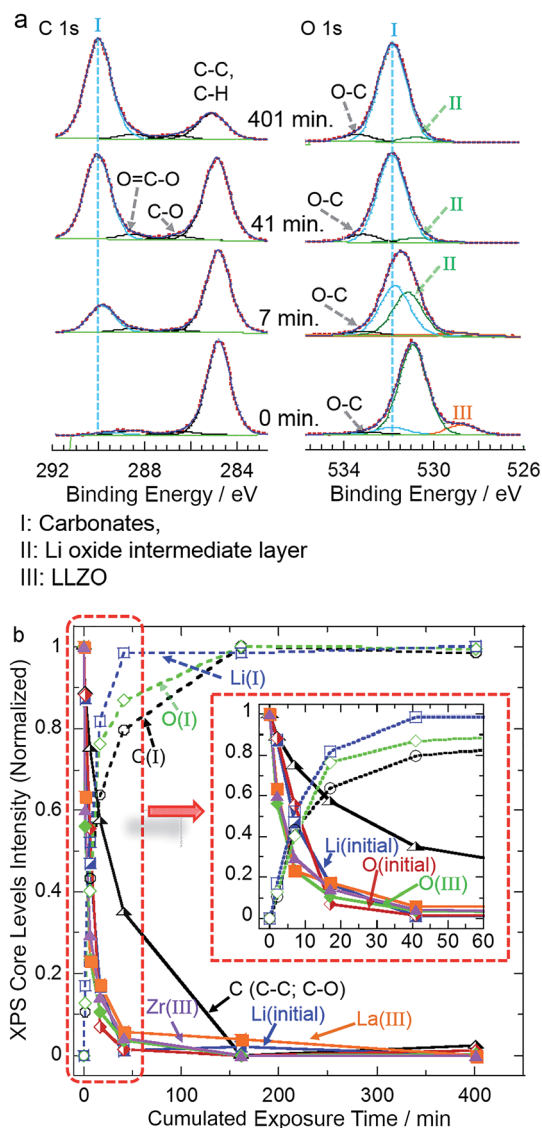


Fig. 6 XPS analysis of LLZO after polishing and exposure to ambient air for various exposure time. (a) C 1s and O 1s, (b) normalized XPS core levels intensity vs. cumulated air exposure time. The inset is a zoom-in on the first 60 minutes of air exposure.

a contamination layer that is thicker than 10 nm (the detection limit for XPS) and this layer was mainly Li_2CO_3 .

3.7 Electrochemical measurements

To evaluate the impact of the contamination layer on the Li-LLZO interfacial resistance electrochemical impedance spectroscopy of Li-LLZO-Li symmetrical cells was performed. The comparison of the impedance spectra for Li-LLZO-Li cells consisting of LLZO exposed to ambient and dry air is shown in Fig. 7. The impedance data were fitted with an equivalent circuit as shown in Fig. 7a. The impedance data of a Li-LLZO-Li cell consists of three distinct constant phase elements (CPE) which were interpreted to represent: Li-LLZO interfacial resistance (R_{int}) between 120 kHz and 1 Hz, grain boundary resistance (R_{gb}), between 1 MHz and 120 kHz; and bulk LLZO resistance

(R_{bulk}), between 7 MHz and 1 MHz. The capacitance values, Q (F), resistance values, and α values were refined from the equivalent circuit modeling for the interfacial resistance, grain-boundary, and bulk transport processes for all samples are shown in Table 2. α is the ideality coefficient for each CPE; the closer to unity, the closer the fit between experimental and idealized behavior.³⁹ The capacitance values should be on the order of 10^{-6} F for the interfacial resistance, 10^{-8} to 10^{-11} F for the grain boundaries, and 10^{-12} F for the bulk transport.^{39,40}

The bulk conductivity of LLZO determined from the high frequency range is largely independent of RH and exposure time. The values are in good agreement with previous studies for bulk Al doped LLZO, which is in the 0.2 to 0.5 mS cm^{-1} range^{41,42} (more details about the effect of air exposure on grain boundary resistance in LLZO can be found in ESI Fig. S4†). The α values for the bulk LLZO and grain boundaries were close to unity and in excellent agreement for all cells, thus confirming the consistency in EIS spectra among all samples. On the other hand, the α values for the interfacial resistance CPEs were less than 0.90 when the LLZO was exposed to air for longer times. This could be a result of the interposition of the contamination layer, which introduced more than one interface CPE, thus deviating from idealized interface resistance. The R_{int} determined for cells containing LLZO with no exposure (b), 24 h (c), 120 h (d), and 240 h (e) exposure to ambient air (RH \sim 50%) showed an increase with exposure time regardless of moisture content (Fig. 7). As expected, the lowest R_{int} was observed for LLZO that was not exposed to air after surface grinding in the glovebox (of $54 \Omega \text{ cm}^2$). This value is the lowest Li-LLZO interface resistance measured using EIS and equivalent circuit modeling.⁴²⁻⁴⁴ After 24 h of exposure, the R_{int} increased by approximately $3\times$ to $145 \Omega \text{ cm}^2$, likely due to the formation of the contamination layer described above. After 120 and 240 h of exposure, the R_{int} further increased to $12\,085 \Omega \text{ cm}^2$ and $36\,782 \Omega \text{ cm}^2$, respectively. Although the DFT could predict the energetics of contamination, the reaction kinetics were too complicated to determine a reaction rate. Further complicating the reaction kinetics was the observation that the Li_2CO_3 cracked, thus likely result in non-uniform Li-LLZO interface contamination rates. Nevertheless, it appeared that R_{int} increased relatively fast in the beginning stages and tapered off at the end, suggesting change in reaction kinetics. To further support the hypothesis that RH affects the kinetics of the contamination reaction, the same exposure time tests were conducted, but in dry air (RH \sim 0.5%). As shown in Fig. 7, R_{int} for LLZO exposed to dry air was considerably lower compared to LLZO exposed to ambient air for the same exposure times (Fig. 7c-e). For example, at 120 h of exposure, the R_{int} in ambient air increased by approximately $10\times$ more than the R_{int} when exposed to dry air. We believe that the higher RH in ambient accelerates the contamination layer growth kinetics compared to dry air.

3.8 Discussion

In this study, the reaction between LLZO and air as a function of RH and time was analysed using DFT calculations and several

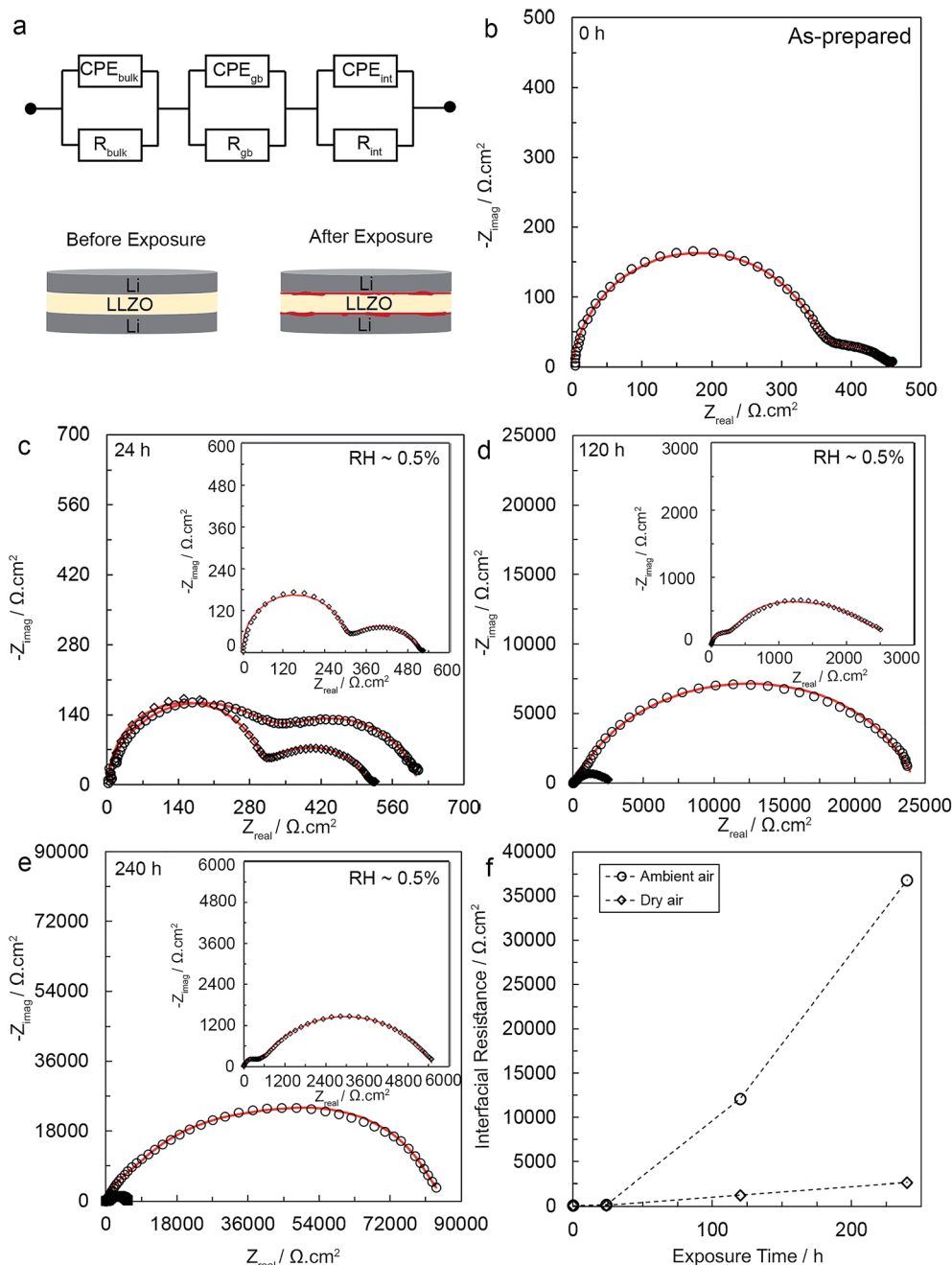


Fig. 7 Impedance spectra measured at room temperature for Li-LLZO-Li cells after various exposure times to ambient (○) and dry air (◇). (a) Schematic depicting the asymmetric Li-LLZO-Li cell before and after air exposure and equivalent circuit modeled used for fitting EIS data, (b) 0 h, (c) 24 h, (d) 120 h, (e) 240 h. The insets show the impedance spectra for Li-LLZO-Li for samples exposed to dry air. Markers indicate experimental data and the solid lines are simulated lines extrapolated from the equivalent circuit modeling, and (e) interfacial resistance at Li-LLZO interface as function of time after exposure to ambient air (○) and dry air (◇), (f) The Li-LLZO interfacial resistance versus time after exposure to ambient and dry air.

materials characterization techniques. DFT calculations determined that LLZO reacts with air resulting in protonation of LLZO and the subsequent formation of LiOH intermediate and Li₂CO₃ contamination layers. Initial XPS measurements were conducted on the LLZO surface after processing in air with no deliberate efforts to limit contamination. The XPS analysis revealed that, LiOH and Li₂CO₃ formed on the LLZO surface,

consistent with the computed reaction thermodynamics. Similar material characterization was performed, but by taking precautions to prevent un-intentional exposure to air such that all reactions were deliberate and controlled. This was accomplished by mechanically cleaning (grinding) LLZO surfaces in an argon glovebox and exposing to air with RH ~0.5 or 50% for specified times up to 240 h. Detailed characterization on LLZO

Table 2 Summary of fitted data for electrochemical impedance spectroscopy of the Li-LLZO-Li symmetric cells

Sample	Q_{bulk} (F)	α_{bulk}	R_{bulk} ($\Omega \text{ cm}^2$)	Q_{gb} (F)	α_{gb}	R_{gb} ($\Omega \text{ cm}^2$)	Q_{inf} (F)	α_{int}	R_{int} ($\Omega \text{ cm}^2$)
0 h	8.3×10^{-12}	1	339	6.6×10^{-8}	0.94	5	1.1×10^{-6}	0.80	54
24 h-RH \sim 50%	4.9×10^{-12}	0.99	310	9.7×10^{-8}	0.96	10	0.5×10^{-6}	0.85	145
120 h-RH \sim 50%	5.8×10^{-12}	0.99	305	4.2×10^{-8}	0.98	30	1.1×10^{-6}	0.77	12 085
240 h-RH \sim 50%	9.8×10^{-12}	0.93	296	8.1×10^{-8}	0.90	120	1.2×10^{-6}	0.87	36 782
24 h-RH \sim 0.5%	8.1×10^{-12}	1	320	4.7×10^{-8}	0.98	6	1.3×10^{-6}	0.89	100
120 h-RH \sim 0.5%	3.6×10^{-12}	1	289	4.3×10^{-8}	0.90	7	1.6×10^{-6}	0.88	1235
240 h-RH \sim 0.5%	2.6×10^{-12}	0.94	380	9.1×10^{-8}	0.92	35	1.6×10^{-6}	0.88	2650

surfaces was performed using SEM/EDS mapping and Raman spectroscopy to study the chemistry of the LLZO surface after exposure to air. SEM micrographs showed the contamination layer formed on the surface was non-uniform. Raman spectroscopy confirmed that the formation of Li_2CO_3 was sensitive to the relative humidity, *i.e.* the higher the relative humidity, the faster the Li_2CO_3 grew. Furthermore, TEM characterization of subsurface LLZO demonstrated that exposure to air resulted in three distinct layers. It was observed that the formation of Li_2CO_3 sequestered Li and possibly O from LLZO, leading to a phase transition immediately below the Li_2CO_3 . Immediately below the intermediate layer, pure LLZO was observed. Additional XPS analyses determined the contamination layer formed in 7 minutes after exposure to ambient air (RH \sim 50%). EIS analysis was conducted to correlate the surface chemistry with R_{int} . As expected, the longer the exposure time and the higher the relative humidity, the higher R_{int} . The practical implications of this work are two-fold. First, R_{int} increases by only a factor of 2 to 3 upon exposure to dry or ambient air for periods up to 24 h. In both cases the resulting interfacial resistances are some of the lowest values reported. This indicates that despite a relatively thin contamination layer that increases R_{int} , LLZO is stable in air. Second, the relatively stable behavior in air suggests that it may be feasible to process LLZO electrolyte membranes and/or solid-state LLZO-based batteries in air, which could reduce manufacturing costs.

4. Conclusion

Understanding the morphology, surface chemistry, and stability of LLZO is essential in the development of next-generation solid-state batteries employing LLZO as solid-state electrolyte. Toward these goals, the present study has examined the effect of air exposure on LLZO surface chemistry and Li-LLZO interfacial resistance. First, DFT calculations were used to evaluate the LLZO air stability. The calculations reveal that LLZO readily reacts with humid air; the most favorable pathway involves protonation of LLZO and formation of an LiOH intermediate. Subsequent exposure to CO_2 (in air) converts the LiOH to Li_2CO_3 . Detailed XPS data showed that LiOH and Li_2CO_3 are present on the LLZO surface after processing in the air. These data agree closely with the results from DFT calculations. Furthermore, SEM analysis indicated the topography changes and non-uniform formation of contamination layer on surface. The extent of Li_2CO_3 formation on LLZO surface has been

shown to depend strongly on RH level and exposure time using Raman spectroscopy. TEM analysis identified the formation of Li deficient LLZO beneath the Li_2CO_3 contamination layer, which is consistent with reaction pathway (3) where LLZO loses Li in exchange for protons. Moreover, the Li-LLZO interfacial resistance was correlated to LLZO surface chemistry. It was shown that the formation of contamination layers at the LLZO surface has a significant effect on the Li-LLZO interfacial resistance. The higher the degree of contamination layer the higher the Li-LLZO interfacial resistance. The results of this work suggest that the LLZO SSE surface has a vital impact on the Li-LLZO interfacial resistance. It has been shown while LLZO can be synthesized, and densified in ambient air, measures must be taken to prevent subtle surface contamination to enable relatively low Li-LLZO interfacial resistance.

Acknowledgements

This work was supported by the U.S. Department of Energy (DOE) Office of Energy Efficiency and Renewable Energy (EERE) Vehicle Technologies Office (VTO) and Advanced Battery Material Research (BMR) program under contract DE-EE 00006821. ORNL contributed to XPS, (MN, JN, HM) and TEM characterization (C. M. and M. C). C. M. and M. C. were supported by the U.S. Department of Energy, Office of Science, Basic Energy Sciences, Materials Sciences and Engineering Division. S. Y. acknowledges support from the Kwanjeong Educational Foundation. A. S. is grateful to Dr Adam J. Matzger (University of Michigan), Dr Nancy Dudney (Oak Ridge National Laboratory) and Dr Jeff Wolfenstine (Army research Laboratory) for valuable discussions.

References

- 1 R. Van Noorden, *Nature*, 2014, **507**, 26.
- 2 R. Murugan, V. Thangadurai and W. Weppner, *Angew. Chem., Int. Ed.*, 2007, **46**, 7778–7781.
- 3 T. Thompson, S. Yu, L. Williams, R. D. Schmidt, R. Garcia-Mendez, J. Wolfenstine, J. L. Allen, E. Kioupakis, D. J. Siegel and J. Sakamoto, *ACS Energy Lett.*, 2017, **2**, 462–468.
- 4 C. Monroe and J. Newman, *J. Electrochem. Soc.*, 2005, **152**, A396–A404.
- 5 S. Zhang, M. S. Ding, K. Xu, J. Allen and T. R. Jow, *Electrochem. Solid-State Lett.*, 2001, **4**, A206–A208.

- 6 P. Liu, J. Wang, J. Hicks-Garner, E. Sherman, S. Soukiazian, M. Verbrugge, H. Tataria, J. Musser and P. Finamore, *J. Electrochem. Soc.*, 2010, **157**, A499–A507.
- 7 D. Aurbach, *J. Power Sources*, 2000, **89**, 206–218.
- 8 M. Broussely, P. Biensan, F. Bonhomme, P. Blanchard, S. Herreyre, K. Nechev and R. Staniewicz, *J. Power Sources*, 2005, **146**, 90–96.
- 9 S. Zhang, K. Xu and T. Jow, *Electrochim. Acta*, 2004, **49**, 1057–1061.
- 10 L. Cheng, E. J. Crumlin, W. Chen, R. Qiao, H. Hou, S. F. Lux, V. Zorba, R. Russo, R. Kostecki and Z. Liu, *Phys. Chem. Chem. Phys.*, 2014, **16**, 18294–18300.
- 11 Y. Shimonishi, A. Toda, T. Zhang, A. Hirano, N. Imanishi, O. Yamamoto and Y. Takeda, *Solid State Ionics*, 2011, **183**, 48–53.
- 12 C. Galven, J. Dittmer, E. Suard, F. o. Le Berre and M.-P. Crosnier-Lopez, *Chem. Mater.*, 2012, **24**, 3335–3345.
- 13 S. Toda, K. Ishiguro, Y. Shimonishi, A. Hirano, Y. Takeda, O. Yamamoto and N. Imanishi, *Solid State Ionics*, 2013, **233**, 102–106.
- 14 W. Xia, B. Xu, H. Duan, Y. Guo, H. Kang, H. Li and H. Liu, *ACS Appl. Mater. Interfaces*, 2016, **8**, 5335–5342.
- 15 Y. Jin and P. J. McGinn, *J. Power Sources*, 2013, **239**, 326–331.
- 16 L. Truong and V. Thangadurai, *Chem. Mater.*, 2011, **23**, 3970–3977.
- 17 L. Truong and V. Thangadurai, *Inorg. Chem.*, 2012, **51**, 1222–1224.
- 18 G. Larraz, A. Orera and M. Sanjuan, *J. Mater. Chem. A*, 2013, **1**, 11419–11428.
- 19 L. Cheng, C. H. Wu, A. Jarry, W. Chen, Y. Ye, J. Zhu, R. Kostecki, K. Persson, J. Guo and M. Salmeron, *ACS Appl. Mater. Interfaces*, 2015, **7**, 17649–17655.
- 20 Z. F. Yow, Y. L. Oh, W. Gu, R. P. Rao and S. Adams, *Solid State Ionics*, 2016, **292**, 122–129.
- 21 G. Kresse and J. Furthmüller, *Phys. Rev. B: Condens. Matter Mater. Phys.*, 1996, **54**, 11169.
- 22 P. E. Blöchl, *Phys. Rev. B: Condens. Matter Mater. Phys.*, 1994, **50**, 17953.
- 23 G. Kresse and D. Joubert, *Phys. Rev. B: Condens. Matter Mater. Phys.*, 1999, **59**, 1758.
- 24 J. P. Perdew, K. Burke and M. Ernzerhof, *Phys. Rev. Lett.*, 1996, **77**, 3865.
- 25 S. Yu, R. D. Schmidt, R. Garcia-Mendez, E. Herbert, N. J. Dudney, J. B. Wolfenstine, J. Sakamoto and D. J. Siegel, *Chem. Mater.*, 2015, **28**, 197–206.
- 26 C. Ma, E. Rangasamy, C. Liang, J. Sakamoto, K. L. More and M. Chi, *Angew. Chem.*, 2015, **127**, 131–135.
- 27 G. Larraz, A. Orera, J. Sanz, I. Sobrados, V. Diez-Gómez and M. Sanjuan, *J. Mater. Chem. A*, 2015, **3**, 5683–5691.
- 28 H. J. Monkhorst and J. D. Pack, *Phys. Rev. B: Solid State*, 1976, **13**, 5188, The Inorganic Crystal Structure Database (ICSD); <https://www.fiz-karlsruhe.de/icsd.html>.
- 29 F. Murnaghan, *Proc. Natl. Acad. Sci. U. S. A.*, 1944, **30**, 244–247.
- 30 M. W. Chase, C. A. Davies, J. R. Downey, D. J. Frurip, R. A. McDonald and A. N. Syverud, *J. Phys. Chem. Ref. Data, Suppl.*, 1985, **14**, 1.
- 31 K. N. Marsh, *Recommended reference materials for the realization of physicochemical properties*, Blackwell Scientific Publications, 1987.
- 32 R. Huggins, *Ionics*, 2002, **8**, 300–313.
- 33 R. Huggins, *Advanced batteries: materials science aspects*, Springer Science & Business Media, 2008.
- 34 A. Boulant, J. F. Bardeau, A. Jouanneaux, J. Emery, J.-Y. Buzare and O. Bohnke, *Dalton Trans.*, 2010, **39**, 3968–3975.
- 35 T. Thompson, J. Wolfenstine, J. L. Allen, M. D. Johannes, A. Huq, I. N. David and J. Sakamoto, *J. Mater. Chem. A*, 2014, **2**, 13431–13436.
- 36 S. Mukhopadhyay, T. Thompson, J. Sakamoto, A. Huq, J. Wolfenstine, J. L. Allen, N. Bernstein, D. A. Stewart and M. Johannes, *Chem. Mater.*, 2015, **27**, 3658–3665.
- 37 F. Tietz, T. Wegener, M. Gerhards, M. Giarola and G. Mariotto, *Solid State Ionics*, 2013, **230**, 77–82.
- 38 J. Tsuji, H. Nakamatsu, T. Mukoyama, K. Kojima, S. Ikeda and K. Taniguchi, *X-Ray Spectrom.*, 2002, **31**, 319–326.
- 39 R. A. Huggins, *Ionics*, 2002, **8**, 300–313.
- 40 J. T. Irvine, D. C. Sinclair and A. R. West, *Adv. Mater.*, 1990, **2**, 132–138.
- 41 T. Thompson, A. Sharafi, M. D. Johannes, A. Huq, J. L. Allen, J. Wolfenstine and J. Sakamoto, *Adv. Energy Mater.*, 2015, **5**, 1500096.
- 42 A. Sharafi, H. M. Meyer, J. Nanda, J. Wolfenstine and J. Sakamoto, *J. Power Sources*, 2016, **302**, 135–139.
- 43 S. Ohta, T. Kobayashi, J. Seki and T. Asaoka, *J. Power Sources*, 2012, **202**, 332–335.
- 44 Y. Kim, A. Yoo, R. Schmidt, A. Sharafi, H. Lee, J. Wolfenstine and J. Sakamoto, *Frontiers in Energy Research*, 2016, **4**, 20.